

1

1

Pupil size reflects activation

2

of subcortical ascending arousal system nuclei during rest

3

4 Beth Lloyd¹, Lycia D. de Voogd^{2,3}, Verónica Mäki-Marttunen¹, Sander Nieuwenhuis¹

5

6 ¹ Institute of Psychology, Leiden University, Leiden, Netherlands

7 ² Donders Institute, Centre for Cognitive Neuroimaging, Radboud University, Nijmegen, The
8 Netherlands.

9 ³ Behavioural Science Institute, Radboud University Nijmegen, The Netherlands.

10

11

12

13

14

15

16

17

18

19

20

21

22

23

24

25

26 **Corresponding author:**

27 Beth Lloyd

28 *Email address:* b.lloyd@fsw.leidenuniv.nl

29 *Address:* Wassenaarseweg 52, 2333 AK Leiden

30

31 **Abstract**

32 Neuromodulatory nuclei that are part of the ascending arousal system (AAS) play a crucial role in regulating
33 cortical state and optimizing task performance. Pupil diameter, under constant luminance conditions, is
34 increasingly used as an index of activity of these AAS nuclei. Indeed, task-based functional imaging studies in
35 humans have begun to provide evidence of stimulus-driven pupil-AAS coupling. However, whether there is such
36 a tight pupil-AAS coupling during rest is not clear. To address this question, we examined simultaneously acquired
37 resting-state fMRI and pupil-size data from 74 participants, focusing on six AAS nuclei: the locus coeruleus,
38 ventral tegmental area, substantia nigra, dorsal and median raphe nuclei, and cholinergic basal forebrain.
39 Activation in all six AAS nuclei was optimally correlated with pupil size at 0- to 2-second lags, suggesting that
40 spontaneous pupil changes were almost immediately followed by corresponding BOLD-signal changes in the AAS.
41 These results suggest that spontaneous changes in pupil size that occur during states of rest can be used as a
42 noninvasive general index of activity in AAS nuclei. Importantly, the nature of pupil-AAS coupling during rest
43 appears to be vastly different from the relatively slow canonical hemodynamic response function that has been
44 used to characterize task-related pupil-AAS coupling.

45

46 **Keywords**

47 Resting-state fMRI; pupillometry; subcortex; locus coeruleus; arousal; hemodynamic response

48

49

50 Introduction

51 Neuromodulatory brainstem, midbrain, and basal forebrain nuclei that together form the core of the
52 ascending arousal system (AAS) are situated deep in the brain. They have widespread projections to the cortex,
53 making them ideally suited to alter cortical states and optimize task performance (Bunzeck & Düz el, 2006; de
54 Gee et al., 2017; Shine et al., 2021; Thiele & Bellgrove, 2018). Pupil diameter, under constant luminance
55 conditions, has vastly been used as a proxy for activity of these subcortical nuclei (Joshi & Gold, 2020). Indeed,
56 task-related activity of these nuclei is accompanied by changes in pupil size and its first-order derivative (i.e., rate
57 of change), as evidenced by animal studies and functional magnetic resonance imaging (fMRI) studies in humans
58 (Cazettes et al., 2021; de Gee et al., 2017; Murphy et al., 2014; Varazzani et al., 2015; Yang et al., 2021). Animal
59 studies have also found pupil-AAS coupling of spontaneous fluctuations during rest (Joshi et al., 2016; Reimer et
60 al., 2016). However, it is still largely unclear whether similar coupling can be found between resting-state
61 fluctuations of pupil size and blood oxygen level-dependent (BOLD) signals in the human AAS. Assessing if and
62 how activity in neuromodulatory brainstem, midbrain, and basal forebrain nuclei can be inferred from pupil size
63 measurements is relevant for promoting our scientific and clinical understanding of AAS function.

64 A small number of human resting-state fMRI studies have investigated the brain activity associated with
65 fluctuations in pupil size (Breed en et al., 2016; Mäki-Marttunen & Espeseth, 2021; Murphy et al., 2014; Yellin et
66 al., 2015) and pupil derivative (DiNuzzo et al., 2019; Schneider et al., 2016). Their results with respect to a
67 coupling between pupil size and AAS activity are inconclusive, with most studies not reporting evidence for such
68 a relationship. However, the majority of these studies did not focus on the AAS. Moreover, they did not include
69 specific localization methods to delineate AAS regions-of-interest (ROIs) or correct for physiological sources of
70 noise, such as cardiac and respiratory fluctuations. These approaches are important for reliable measurements
71 in these subcortical nuclei (Brooks et al., 2013; Matt et al., 2019). To date, only Murphy et al. (2014) specifically
72 investigated the relationship between pupil size and one AAS nucleus, namely the locus coeruleus (LC). The
73 authors found a positive coupling between fluctuations in pupil size and activation in the LC during rest. To our
74 knowledge, there have been no human fMRI studies so far that have reported a relationship between pupil size
75 and other AAS nuclei during rest, despite the growing evidence from animal studies (Joshi et al., 2016; Reimer et
76 al., 2016) speaking for such a relationship. Therefore, in the current study, we aimed to investigate whether pupil
77 size (and the pupil derivative) can be used as an index of activity in neuromodulatory AAS nuclei during rest.

78 To address this aim, we systematically examined simultaneous measurements of resting-state fMRI and
79 pupil size from a large sample of healthy adults (N=74). We monitored BOLD signal from a number of subcortical
80 nuclei part of the AAS and implicated in the control of cortical arousal levels: the LC, the ventral tegmental area
81 (VTA), dopaminergic substantia nigra (SN), the dorsal (DR) and median (MR) raphe nuclei and the nucleus basalis
82 of Meynert in the cholinergic basal forebrain (BF). Due to their size and location in the brain, studying these small
83 nuclei using fMRI comes with a unique set of challenges (Forstmann et al., 2017; Liu et al., 2017a; Matt et al.,
84 2019). Here, we mitigated these challenges by implementing a number of methods, including multi-echo imaging
85 to increase signal-to-noise ratio in subcortical structures (Miletić et al., 2020; Puckett et al., 2018; Turker et al.,
86 2021), neuromelanin-weighted T1 imaging for delineation of the LC (Clewett et al., 2016; Keren et al., 2015; Mäki-

87 Marttunen & Espeseth, 2021; Priovoulos et al., 2018), optimized brainstem co-registration (ANTs SyN; Ewert et
88 al., 2019), physiological noise regression to suppress respiratory and cardiac artifacts (Glover et al., 2000; Harvey
89 et al., 2008), and no spatial smoothing of fMRI data (de Gee et al., 2017).

90 As a first analysis, we intended to reproduce the analyses from two previous studies that did (Murphy
91 et al., 2014) and did not (Schneider et al., 2016) find AAS correlates of pupil size during rest. The analyses in these
92 studies were performed under the assumption that the relationship between pupil size and resting-state BOLD
93 activity in AAS nuclei is governed by the canonical hemodynamic response function (HRF). As we could not
94 replicate previous findings, we reasoned it is possible that during rest, when there is no external stimulus driving
95 neural activity, the temporal relation between pupil dilation and AAS activity does not follow an HRF-like
96 waveform. Therefore, we began examining the temporal relationship between pupil time series and AAS-BOLD
97 activation using various transfer functions based on the canonical HRF, taking into account that subcortical
98 structures have been characterized by faster time-to-peak (TTP) of the HRF than the cortex (Lau et al., 2011;
99 Lewis et al., 2018; Yen et al., 2011). It is possible that the HRF does not provide an adequate model of the
100 relationship between resting-state fluctuations in pupil size and AAS BOLD activity. We therefore also explored
101 cross-correlations between AAS BOLD activity and the unconvolved pupil time series, systematically varying the
102 forward and backward lag between the two measures. Together, these analyses offer new insights into the use
103 of pupil size as an index of activity in AAS regions.

104

105 **Results**

106 The Results section is organized as follows. We first report a couple of verification analyses aimed to
107 ensure that we could replicate the resting-state correlations between pupil size and whole-brain BOLD patterns
108 reported in previous studies, and to assess the signal quality within the subcortical nuclei. Then, we attempt to
109 reproduce the pupil-LC coupling that was reported in Murphy et al. (2014) by applying their convolution approach
110 and LC localization method, as well as by interrogating the signal within our group LC ROI. After this, we move
111 on to report three key analyses of pupil-AAS coupling aimed at understanding the temporal relationship between
112 the two as well as the nature of this relationship: (i) an analysis in which we account for region- and participant-
113 specific HRF differences in the convolution approach of the pupil time series; (ii) an analysis in which we explore
114 pupil-AAS coupling while systematically adjusting the TTP of the HRF; and (iii) a cross-correlation analysis and
115 cross spectral power density analysis in which we explore the possibility that, during rest, the temporal
116 relationship between pupil size and AAS BOLD patterns is not mediated by the HRF typically used in event-related
117 fMRI design.

118

119 ***Whole-brain pupil-BOLD patterns consistent with previous studies***

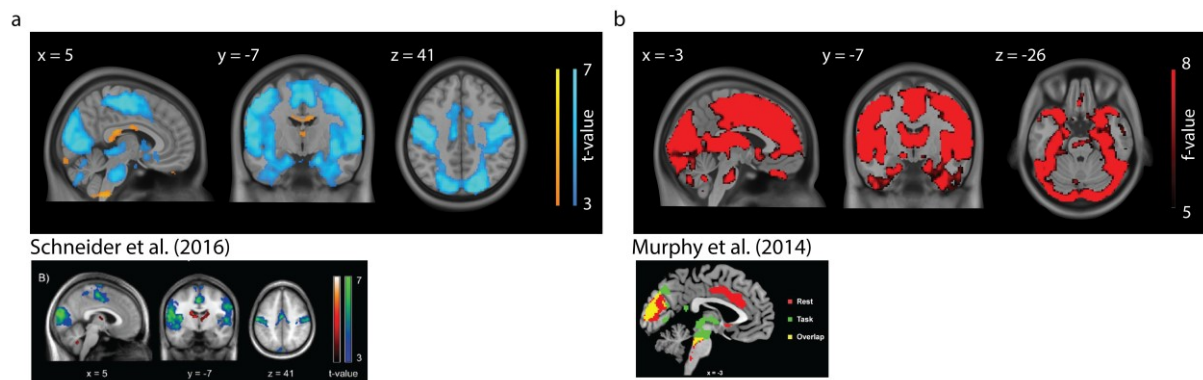
120 We aimed to verify that our data showed the expected pupil-associated BOLD response patterns at the
121 level of the cortex, cerebellum and subcortical parts of the limbic system. To this end, we followed as closely as

5

122 possible the approaches from two previous studies reporting pupil-BOLD coupling during rest (Murphy et al.,
123 2014; Schneider et al., 2016) and indeed largely replicated their findings. First, following the approach by
124 Schneider et al. (2016), we used pupil size (1-s shift) as a regressor in a GLM and convolved it with the canonical
125 HRF (i.e., 6-s TTP). The assumption here is that the neural activity associated with spontaneous changes in pupil
126 size is transformed into resting-state BOLD signal according to the same impulse response function as that driving
127 neurovascular coupling during task performance. Indeed, we found positive correlations in the thalamus and
128 negative correlations in the visual cortex and sensorimotor areas, as well as in the precuneus, cuneus, insula,
129 superior temporal gyrus, and parahippocampal gyrus. These patterns of activation are consistent with those
130 reported by Schneider et al. (2016; Figure 1a and Table 1). Second, we carried out the analysis in line with Murphy
131 et al. (2014), using pupil size (not shifted) as a regressor and convolving it with the canonical HRF (i.e., 6-s TTP)
132 as well as its temporal and dispersion derivatives (Figure 1b and Table 2). Adding these derivatives allows the
133 timing of the HRF response peak and the width of the HRF response to vary across the whole brain. Here, we
134 found significant clusters in the visual cortex, the insula, the anterior cingulate gyrus, and the inferior frontal
135 gyrus, consistent with what was reported by Murphy et al. (2014). Overall, we found pupil-related BOLD response
136 patterns across the whole brain that were highly consistent with the ones reported by the previous two studies.

137 Following Murphy et al.'s. (2014) approach, we also inspected pupil-associated activity in the LC. However, we
138 did not find significant voxels when using our group LC mask as an ROI or when we applied the more liberal mask
139 used by (2014; Keren et al., 2009; 2-SD version). Thus, contrary to Murphy et al. (2014), we were unable to
140 replicate pupil-LC BOLD coupling using the same convolution methods.

141



142

143 **Figure 1. Whole-brain pupil-BOLD coupling in comparison to previous studies.** Neural correlates of pupil size
144 from the analysis using the convolution approach from (a) Schneider et al. (2016) and (b) Murphy et al. (2014).
145 Note that we only refer to the red and yellow activation in the figure from Murphy et al. (2014). Statistical
146 parametric maps are thresholded at $p < .001$, uncorrected, for visualization purposes only. Whole-brain cluster-
147 level FWE-corrected inferential statistics, in MNI space, are reported in Table 1 and 2.

148

149

150 **Table 1.** Regions showing pupil-BOLD coupling using the convolution methods from Schneider et al. (2016)

	Cluster	
	K	p_{corr}
<i>Positive</i>		
Thalamus (R), Posterior cingulate cortex (R/L)	871	<.001
Rectus (L)	199	.010
Cerebellum (R)	142	.043
Cerebellum crus (L)	250	.003
<i>Negative</i>		
Cerebellum crus (R/L), cerebellum 6 (R/L), cerebellum 4/5 (R/L), (lingual gyrus (R/L), calcarine (R/L), fusiform gyrus (R/L), cuneus (R/L), precuneus (R/L), cerebellum 4 + 5 (L), cerebellar vermis, hippocampus (R/L), parahippocampal gyrus (R), amygdala (R/L), thalamus (R), superior occipital gyrus (R/L), middle occipital gyrus (R/L), inferior occipital gyrus (R/L), superior parietal gyrus (L), inferior temporal gyrus (R/L), middle temporal gyrus (R/L), superior temporal gyrus (R/L), insula (R), postcentral gyrus (L), precentral gyrus (L), paracentral lobule (R/L), supplementary motor area (R/L), middle cingulate gyrus	65223	<.001

151 *Note. Reported clusters survived whole-brain family-wise error (FWE) correction at the cluster level ($p_{FWE} = .05$). Abbreviations: R = right, L =*
 152 *left, p_{corr} = whole brain corrected cluster p-values, k = cluster size.*

153

154 **Table 2.** Regions showing pupil-BOLD coupling using convolution methods from Murphy et al. (2014)

	Cluster	
	K	p_{corr}
Middle occipital gyrus (R/L), superior occipital gyrus (R/L), calcarine gyrus (R/L), cuneus (R/L), precuneus (R/L), angular gyrus (R/L), fusiform gyrus (R/L), cerebellum (R/L), middle temporal pole (R/L), inferior temporal pole (L), insula (R), inferior parietal lobule (R/L), superior parietal lobule (L), postcentral gyrus (R/L), middle frontal gyrus (R/L), medial frontal gyrus (R/L), inferior frontal gyrus (R/L), superior frontal gyrus (R/L), posterior cingulate gyrus, middle cingulate gyrus, anterior cingulate gyrus, supplementary motor area (R/L), middle frontal orbital (R/L), inferior frontal orbital (R/L), cerebellum crus II (R/L), cerebellum crus I (R/L), cerebellum 8 (R/L), cerebellum 9 (R/L), Pons	91471	<.001
Rectus (R/L)	146	.010

155 *Note. Reported clusters survived whole-brain family-wise error (FWE) correction at the cluster level ($p_{FWE} = .05$). Abbreviations: R = right, L =*
 156 *left, p_{corr} = whole brain corrected cluster p-values, k = cluster size.*

157

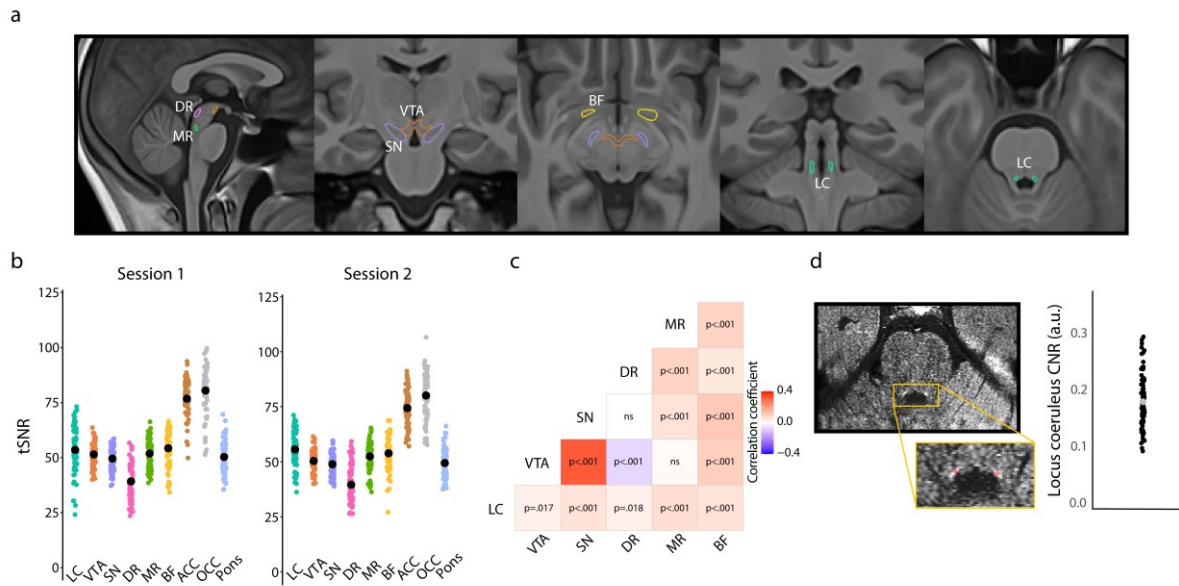
158 **Assessment of the quality of subcortical fMRI data**

159 To assess the quality of the subcortical functional data we extracted the tSNR from each ROI (see
 160 *Methods*). The average tSNR across the AAS ROIs (Figure 2b; range: 23.3 - 72.9) and cortical regions (range: 49.6
 161 - 106.3) were in line with previous reports (Brooks et al., 2013, Figure 1: brainstem range: ~1-50 and cortex range
 162 ~50-112; Sing et al., 2022, supplementary Figure 6: brainstem range: 0-50, cortex range: 0-50). We also replicated
 163 a recently reported pattern of positive (partial) correlations among the signal fluctuations in each pair of

7

164 subcortical ROIs, controlled for activity in the pons (Figure 2c; van den Brink et al., 2019; see also Singh et al.,
 165 2022). Only the correlation between the DR and VTA was negative. Therefore, we are confident that the data
 166 had sufficient tSNR in our AAS ROIs to be able to assess pupil-AAS coupling.

167



168

169 **Figure 2. Overview of region-of-interest definition and validation of the quality of subcortical fMRI data.** (a) All
 170 subcortical ROIs overlaid on the group T1 template. (b) Individual data points showing the temporal signal-to-
 171 noise ratio for each ROI for session 1 (left) and session 2 (right; black points indicate the mean). (c) Correlation
 172 matrix showing that activity in subcortical nuclei co-varied positively with activity in other subcortical nuclei, with
 173 the strongest coupling present between the VTA and SN, which is to be expected given their close proximity, and
 174 the weakest (negative correlation) between the VTA and DR. Note: correlations were FDR-corrected and
 175 controlled for activity in the pons. (d) FSE image of an example participant. Hyperintensities corresponding to the
 176 LC are visible in the yellow box (top). Using the FSE images, the LC (red) was manually delineated on the individual
 177 level following established protocols (Clewett et al., 2016; Mather et al., 2017). The graph shows the LC contrast-
 178 to-noise ratio for all participants. The grey dot indicates the grand mean. Abbreviations: LC – locus coeruleus, VTA
 179 – ventral tegmental area, SN – substantia nigra, DR – dorsal raphe, MR – medial raphe, BF – basal forebrain ACC
 180 – anterior cingulate cortex, OCC – calcarine sulcus, CNR – contrast-to-noise ratio.

181

182

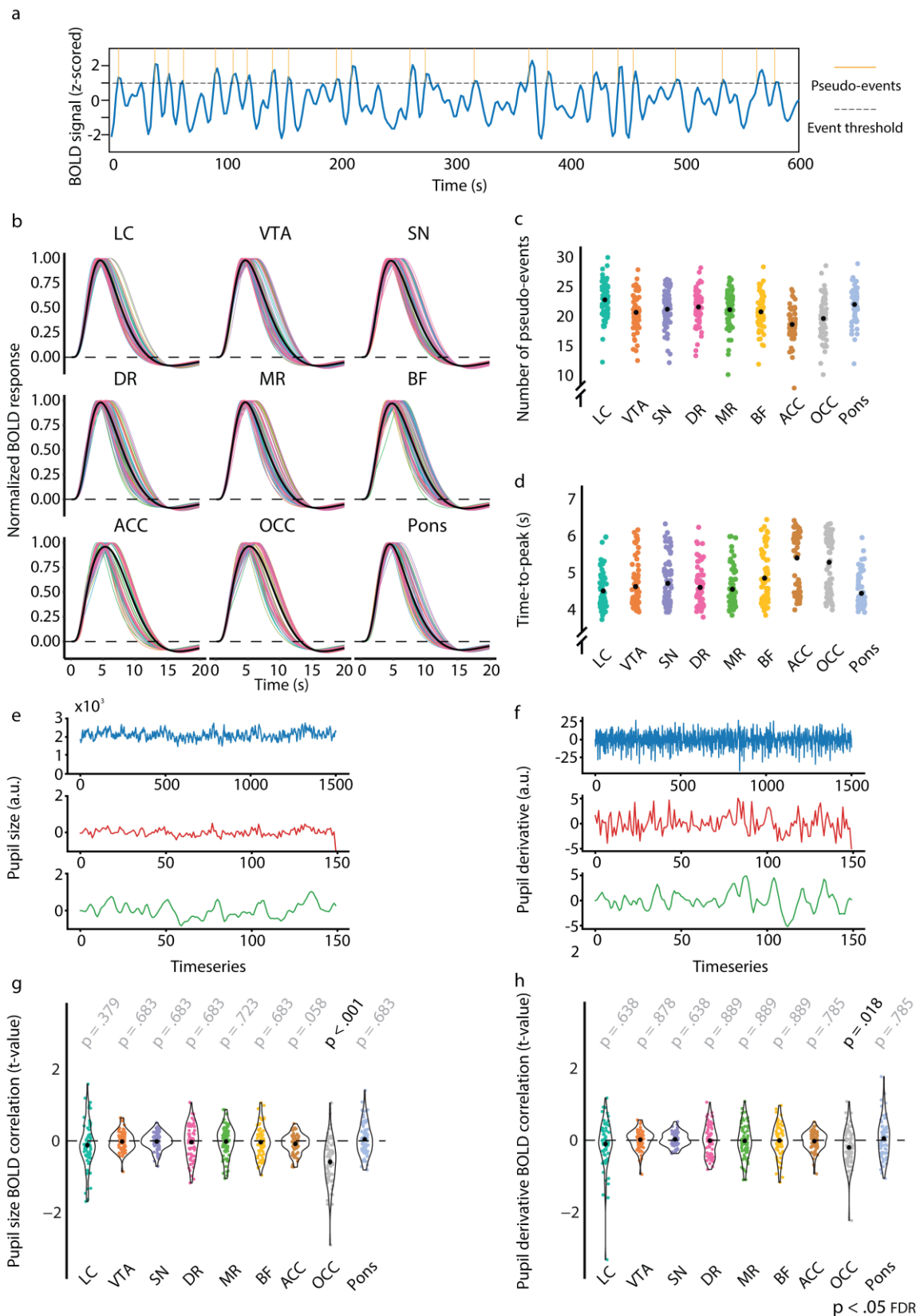
183 **No pupil-AAS coupling using region- and participant-specific estimates of the HRF**

184 The methods that have previously been used to examine co-fluctuations between pupil size and fMRI
 185 BOLD patterns worked under the assumption that the shape of the HRF during rest is homogeneous across the
 186 whole brain (Breedon et al., 2016; DiNuzzo et al., 2019; Schneider et al., 2016; Yellin et al., 2015). This assumption

187 may not be correct, and because even a 1-s latency difference between assumed HRF and actual HRF can have a
188 significant impact on fMRI results (Wall et al., 2009), it may be important to account for regional and individual
189 differences (Handwerker et al., 2004) in the shape of the HRF. Indeed, subcortical structures have been
190 characterized by faster BOLD responses (TTP 4 – 5 s; Lau et al., 2011; Lewis et al., 2018; Yen et al., 2011) compared
191 to the cortex (TTP 5 – 6 s; Lewis et al., 2018; Friston et al., 2000). Therefore, we next estimated ROI-specific and
192 participant-specific HRFs using an approach in which spontaneous pseudo-events were identified in our resting-
193 state data and then aligned to determine the delay between the pseudo-events and corresponding BOLD
194 signatures (Rangaprakash et al., 2018; Wu et al., 2013). The number of detected pseudo-events per ROI is shown
195 in Figure 3c. Note that for some participants only one session was used to estimate these HRFs, so the number
196 of detected pseudo-events for these participants tended to be smaller.

197 After carrying our pairwise comparisons, we found that, as expected, the TTP of the estimated HRFs was
198 significantly faster for all subcortical AAS ROIs than for each of the two cortical ROIs ($M_{\text{subcortical ROIs}} = 4.7$ s,
199 $SD_{\text{subcortical ROIs}} = 0.6$ s, $M_{\text{cortical ROIs}} = 5.4$ s, $SD_{\text{cortical ROIs}} = 0.8$ s; Figure 3d). The pupil-BOLD analysis using these specific
200 HRFs, however, revealed no significant pupil-AAS correlations (Figure 3g, 3h). We only found that pupil size
201 correlated negatively with activation in the OCC ($p_{\text{corr}} < .001$ [pupil size], $p_{\text{corr}} = .018$ [pupil derivative], FDR-
202 corrected). Note that the negative sign of this correlation is consistent with what we reported above and with
203 previous reports linking pupil size to decreased activity in the visual system (Schneider et al., 2016; Yellin et al.,
204 2015).

9



205

206 **Figure 3. Overview of the analysis using region- and participant-specific estimates of the HRF.** (a) One
 207 participant's pre-processed LC BOLD signal (concatenated across the two sessions), evaluated against a chosen
 208 threshold (>1 SD) to extract onsets of spontaneous neural events (indicated in yellow). (b) Estimated
 209 hemodynamic response functions (HRFs) for each participant and ROI. Black lines indicate the average across

210 participants. (c) The number of spontaneous neural events that were used to estimate the region- and participant-
211 specific HRFs. Black dots indicate the mean. (d) Time-to-peak (TTP) of the HRF for each participant and ROI. Black
212 dots indicate the average across participants. Overview of the pupil data processing pipeline of one randomly
213 chosen participant for pupil size (e) and the pupil derivative (f). The plots portray the raw pupil data (blue), the
214 pupil time series down-sampled to the TR (red), and the convolved pupil time series (for LC HRF, green). The
215 extracted *t*-values from the first-level resting-state HRF analysis for pupil size (g) and the pupil derivative (h). *P*-
216 values refer to one-sample *t*-tests (difference from zero; FDR-corrected). Abbreviations: LC – locus coeruleus, VTA
217 – ventral tegmental area, SN – substantia nigra, DR – dorsal raphe, MR – median raphe, BF – basal forebrain, ACC
218 – anterior cingulate cortex, OCC – calcarine sulcus.

219

220 In sum, the use of region- and participant-specific HRFs also did not result in significant pupil-AAS
221 coupling. Importantly, by focusing on pseudo-events in the fMRI data, this approach still assumes that
222 neurovascular coupling during rest (and other passive conditions) is characterized by the typical sluggish HRF
223 used in event-related fMRI design.

224

225 **Positive pupil-AAS coupling using HRFs with rapid time-to-peaks**

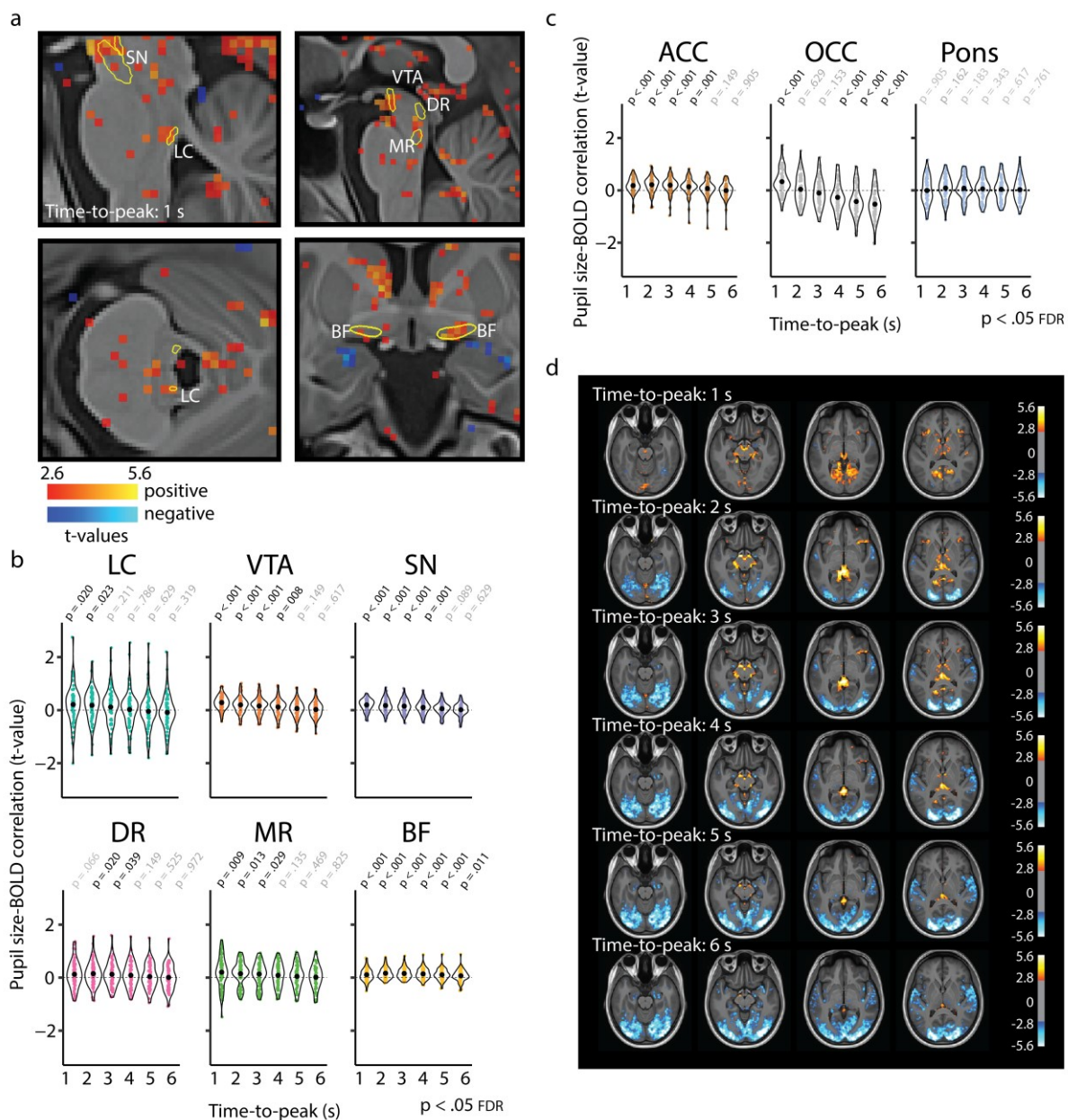
226 Since the analysis strategy so far unexpectedly did not result in pupil-AAS coupling, we let go of the
227 assumption of a relatively slow HRF similar to that driving neurovascular coupling during task performance.
228 Therefore we further examined a potential relationship between pupil and AAS ROIs by examining how
229 *systematically* varying the TTP (from 1 s to 6 s) of the default canonical HRF affected the coupling between pupil
230 dynamics and our AAS ROIs. This analysis was inspired by a recent animal study (Pais-Roldán et al., 2020) showing
231 that pupil-BOLD signal coupling dynamics vary across time.

232 We found that for almost all AAS ROIs the strength of pupil-BOLD coupling differed across TTPs (main
233 effect of TTP; LC: $p < .001$, VTA: $p < .001$, SN: $p < .001$, MR: $p = .043$, BF: $p = .009$, FDR-corrected for nine ROIs).
234 The overall pattern shows that coupling between pupil size and AAS BOLD patterns increases with earlier TTPs.
235 Specifically, we found positive correlations for all AAS regions at earlier TTPs (especially the 1-s [Figure 4a] and
236 2-s TTPs) but no significant correlations (LC, VTA, SN, DR, MR) at later TTPs (5 s to 6 s; Figure 4b). For the OCC
237 ROI, we found a positive correlation at the 1-s TTP, followed by a shift to negative correlations at later TTPs (4 s
238 to 6 s), which is in line with previous work (Breedon et al., 2016; Schneider et al., 2016; Yellin et al., 2015) and
239 the results we reported above (*Whole-brain pupil-BOLD patterns consistent with previous studies*), whereas the
240 ACC correlated positively with pupil size at predominantly early TTPs (1 s to 4 s; Figure 4c; 4d), similar to the AAS
241 ROIs.

242 Similar analyses for the pupil derivative also showed significant differences in the strength of pupil-BOLD
243 coupling across the TTPs for the VTA ($p = .012$), SN ($p = .022$), DR ($p = .002$), ACC ($p = .009$), and OCC ($p < .001$;
244 FDR-corrected for nine ROIs). The overall pattern and follow-up *t*-tests revealed similar, but attenuated effects

245 in comparison to pupil size (Figure S2a). The most prominent exception was the OCC, which showed a curvilinear
246 relationship with largest correlations for intermediate TTPs (2s to 5s), which is also visible upon inspecting the
247 whole-brain maps in Figure S2b. The same analyses carried out for the control region in the pons revealed no
248 main effect of TTP for pupil size or the pupil derivative, nor were there any positive or negative associations with
249 pupil size or the pupil derivative for any TTP, attesting to the specificity of the pupil-BOLD associations found in
250 our AAS and cortical ROIs. Statistical parametric maps including whole brain results for all TTPs are shown in
251 Figure 4d and Figure S2b.

252 These exploratory analyses suggest that fluctuations in pupil diameter have a much closer temporal
253 relationship with changes in AAS-BOLD activity than what is characteristic of event-related responses.



256 **Figure 4. Pupil-BOLD correlations based on systematic adjustment of the time-to-peak of the HRF.** (a) Statistical
 257 maps showing pupil-BOLD correlations in the subcortex for the 1-s TTP. Graphs show the extracted t-statistics as
 258 a function of the systematically adjusted TTP for each participant in the subcortical ROIs (b) and the validation
 259 and control ROIs (c). P-values refer to one-sample t-tests (difference from zero; FDR-corrected). Black dots indicate
 260 the mean. (d) Statistical maps showing unsmoothed pupil-BOLD correlations across the cortex for each TTP (1 s
 261 to 6 s). All statistical maps were thresholded at $p < .005$ (uncorrected) for visualization purposes only.
 262 Abbreviations: LC – locus coeruleus, VTA – ventral tegmental area, SN – substantia nigra, DR – dorsal raphe, MR
 263 – median raphe, BF – basal forebrain, ACC – anterior cingulate cortex, OCC – calcarine sulcus.

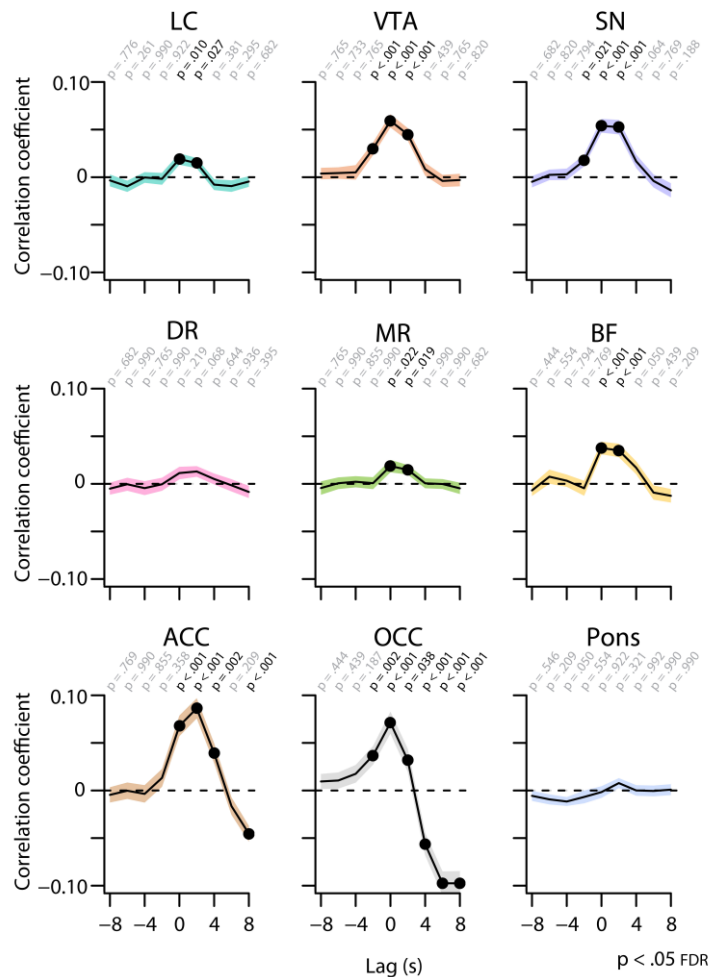
265 ***Positive pupil-AAS coupling when BOLD patterns closely follow pupil fluctuations***

266 In our next analysis we wanted to release the assumption that BOLD responses associated with pupil-
267 size changes would resemble an HRF. Therefore, we correlated the BOLD signal from our AAS ROIs with the
268 *unconvolved* pupil vector using a cross-correlation approach (Pais-Roldán et al., 2020; Yellin et al., 2015). This
269 method also allowed us to interrogate the pupil-BOLD coupling in both time directions. To that end, we shifted
270 the pupil vector 8 s backwards and forwards, in steps of 2 s, with negative lags (backwards) corresponding to
271 pupil changes preceding the BOLD signal, and positive lags (forwards) corresponding to pupil changes succeeding
272 the BOLD signal (Figure 5).

273 Critically, and in line with the TTP analysis, we found significant positive pupil-BOLD correlations for all
274 AAS ROIs (except the DR), with the strongest correlations occurring at lag 0 (Figure 5). These results again suggest
275 that the relationship between pupil size and AAS activity is temporally close, rather than following the shape of
276 an HRF with a 5- or 6-s TTP. In addition, these patterns of results appeared to be stable across the two sessions
277 (Figure S3). For the pupil derivative (Figure S4), we observed a similar pattern in SN and VTA, with stronger
278 correlations at lag 0, although overall the correlation coefficients were attenuated compared to those for pupil
279 size, or not present in some AAS ROIs (LC, MR, and BF).

280 For comparison, we also computed cross-correlations between pupil size and BOLD signal extracted
281 from our validation and control ROIs (ACC, OCC, pons; Figure 5). The OCC showed strong negative correlations at
282 lags +4 to +8 s, similar to previous studies (Murphy et al 2014; Schneider et al 2016), and in line with the
283 replication and TTP analyses reported above. However, the OCC also showed a positive correlation with pupil
284 size at short lags (-2 s to +2 s). Similarly, we found that both ACC and OCC correlated most strongly with the pupil
285 derivative (Figure S4) at relatively short positive lags (0 s to +4 s), with a shift to a strong negative correlation at
286 maximum positive lags (+8 s), especially in the OCC.

287 Together, the TTP analysis and cross-correlation analysis yield essentially the same outcome, suggesting
288 that no HRF convolution is needed to characterize the relationship between pupil size and AAS BOLD patterns
289 during rest.



290

291

292

293

294

295

296

297

Figure 5. Cross-correlations between the unconvolved pupil time series and the BOLD time series at various time lags. Negative (positive) time lags indicate that the pupil signal precedes (follows) the BOLD signal. Black lines indicate the grand mean and shaded regions indicate the standard error of the mean. P-values refer to one-sample t-tests for the corresponding time bin. Black font and black dots indicate significant time bins ($p < .05$, FDR-corrected).

Pupil-AAS coupling is largely driven by oscillations in low-frequency band

298

299

300

301

302

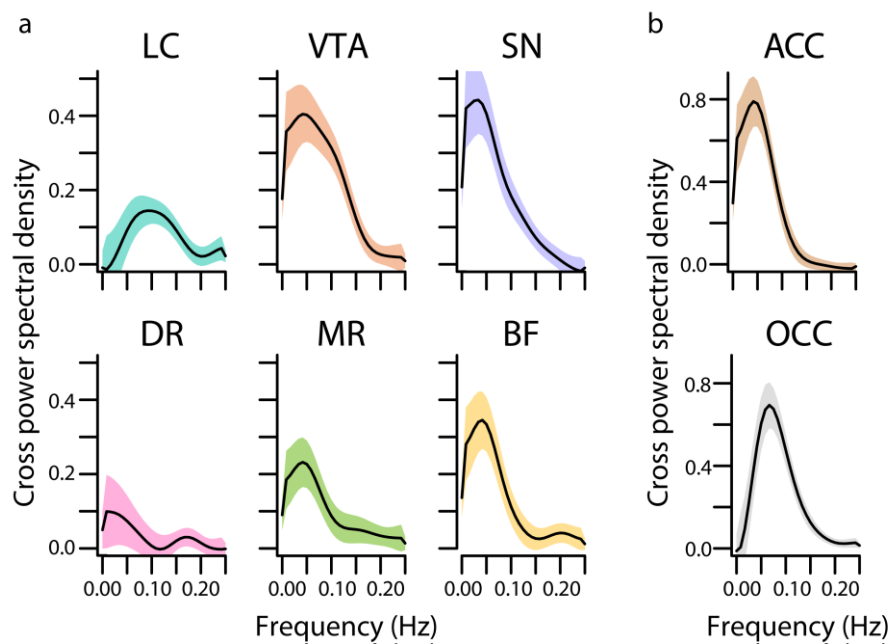
303

304

305

Finally, to better understand the nature of the pupil-AAS coupling, we carried out an exploratory cross-spectral density analysis (Figure 6). The cross power spectral density is the Fourier transform of the cross-correlation functions reported above, and hence expresses the relationship between the pupil and AAS signals in the frequency domain. To determine which frequency bands were driving the observed positive pupil-AAS correlations, we calculated the cross spectral power density (see *Methods*) of the pupil size time series and average BOLD time series extracted from each ROI. A simple peak detection indicated that the correlations for most AAS nuclei and both cortical ROIs (ACC and OCC) were largely driven by frequencies between 0.04 and 0.09 Hz (LC: 0.09, VTA: 0.04, SN: 0.03, DR: 0.008, MR: 0.04, BF: 0.04, ACC: 0.04, OCC: 0.07; Figure 6a; 6b).

306



307

308

309

310

311

312

313

314

315 Discussion

316

317

318

319

320

321

322

323

324

325

326

327

328

329

Figure 6. Cross spectral power density analysis. Cross spectral power density for subcortical ROIs (a) and cortical ROIs (b) averaged across participants. Black lines indicate the grand mean and shaded regions indicate the standard error of the mean. Abbreviations: LC – locus coeruleus, VTA – ventral tegmental area, SN – substantia nigra, DR – dorsal raphe, MR – median raphe, BF – basal forebrain, ACC – anterior cingulate cortex, OCC – calcarine sulcus.

In the current study we examined whether, during rest, non-luminance-related spontaneous fluctuations in pupil size were associated with fluctuations in BOLD signal in nuclei part of the ascending arousal system (AAS). We found a positive correlation between pupil size and BOLD signal in all of the AAS ROIs: LC, VTA, SN, DR, MR and (sublenticular) BF. This finding is in line with recent rodent studies (Joshi et al., 2016; Reimer et al., 2016) indicating that pupil changes reflect activity in multiple neuromodulatory systems, not only the noradrenergic system. Critically, using two different methodological approaches, we found that pupil-AAS coupling was strongest when the two signals were assumed to occur close in time. This means that during rest, unlike in response to task events (de Gee et al., 2017), BOLD signal fluctuations in AAS nuclei immediately follow fluctuations in pupil size. This correlation was largely driven by slow oscillations (i.e., ~0.05 – 0.1 Hz) in both measures. Together, our results suggest that pupil size can be used as a noninvasive readout of AAS activity, and reveal new insights into the temporal dynamics of pupil-AAS coupling during rest.

We found robust positive correlations between pupil size and BOLD signal in five of our AAS ROIs: LC, VTA, SN, MR and (sublenticular) BF. The positive relationship with pupil size was less robust for the DR, and only

330 significant in the TTP analyses, perhaps because this area had lower tSNR than the other subcortical ROIs. Thus,
331 unlike what findings from previous studies (e.g., Murphy et al., 2014) may have implicitly suggested, the coupling
332 between pupil size and activation of the AAS is not specific for the LC. Our findings contribute to a growing body
333 of literature showing a more general role for AAS nuclei in driving pupil size changes. Specifically, our findings
334 are consistent with recent animal studies that found co-fluctuations in pupil size and LC and BF activity during
335 rest (Joshi et al., 2016; Reimer et al., 2016); with studies showing that optogenetic activation of the LC or DR
336 increases pupil size (Breton-provencher & Sur, 2019; Cazettes et al., 2021); and with human task-related fMRI
337 work showing positive correlations between event-related pupil responses and BOLD responses in the LC, VTA
338 and BF (de Gee et al., 2017). Unfortunately, it has become common practice for researchers to interpret task-
339 related pupillometry data in terms of the role of the LC in cognitive and brain function. However, our findings
340 reinforce previous arguments (Joshi & Gold, 2020) that changes in pupil size should not be used to infer a
341 selective role for the LC. An outstanding question is to what extent the AAS nuclei have *independent* influences
342 on pupil size.

343

344 The temporal relationship between pupil size and AAS BOLD response patterns was different than we
345 had expected based on reports from previous resting-state and event-related fMRI studies (e.g., de Gee et al.,
346 2017; Murphy et al., 2014). Namely, we found that BOLD signal in the AAS closely followed the corresponding
347 pupil fluctuations. These results were corroborated by a series of analyses in which we convolved the pupil time
348 series with HRFs with systematically varied TTP (1-6 s). Pupil time series that were convolved with the canonical
349 HRF (TTP = 6 s) or region-specific HRFs based on a point process approach were not significantly related to AAS
350 activation. Instead, maximal and significant pupil-AAS coupling was found using HRFs with TTPs of 1 to 3 seconds.
351 In addition, cross-correlations between the unconvolved pupil time series and AAS BOLD time series similarly
352 revealed maximum correlations when the signals occurred close in time (at lags of 0 to 2 seconds). For the pupil
353 derivative we obtained similar results, with strongest cross-correlations around lag 0 s to +2 s, although the
354 correlation coefficients were overall attenuated and only remained significant in the VTA and SN. Our findings
355 are in line with previous research that has suggested that subcortical regions (Lewis et al., 2018) and AAS nuclei
356 (de Gee et al., 2017) are characterized by faster event-related hemodynamic responses than cortical regions.
357 However, our findings suggest an even closer temporal relationship between pupil size and BOLD response
358 patterns in AAS nuclei during rest. Therefore, these findings, although correlational, have implications for our
359 understanding of the time scale at which AAS regions might drive changes in pupil diameter.

360

361 Furthermore, our findings may provide a reason why most previous human resting-state pupil-fMRI
362 studies (e.g. Breeden et al., 2016; Schneider et al., 2016; Yellin et al., 2015) did not find or report pupil-AAS
363 coupling. Namely, these studies only investigated pupil-BOLD coupling with longer time lags between pupil
364 changes and corresponding BOLD response patterns. Using standard TTPs we (broadly) replicated previously
365 reported associations between pupil size and cortical BOLD response patterns (e.g., negative coupling with the
366 visual cortex, positive coupling with the thalamus and posterior cingulate cortex; e.g., Murphy et al., 2014;
367 Schneider et al., 2016; Yellin et al., 2015). However, we did not find evidence that standard TTPs characterized

368 the coupling between resting-state pupil size and AAS activation. Although one of these previous studies did
369 report pupil-LC coupling (Murphy et al., 2014), we were unable to replicate this finding in our data, despite using
370 the same convolution methods, LC mask, and other methodological details of this study, and despite a much
371 larger sample size (70 versus 14 included participants). Although we cannot make a direct comparison between
372 the shape of human and mouse HRFs, a recent study in rats (Pais-Roldán et al., 2020) also found temporally close
373 positive coupling (i.e., 1-s TTP) between resting-state pupil dynamics and BOLD signal in specific areas in the
374 brainstem including the A5 noradrenergic cell group (which projects to the spinal cord). They, however, did not
375 find evidence for a coupling between pupil dynamics and any of the AAS nuclei. Although this seems inconsistent
376 with our findings, note that the rats in this study were anesthetized. Indeed, preliminary evidence suggests that
377 behavioral states can strongly modulate pupil-AAS coupling (Megemont et al., 2022), and therefore it is possible
378 that in an anesthetized state pupil-AAS coupling is reduced or absent.

379

380 Lastly, our findings raise the question *how* the neuronal activity in AAS nuclei that contributes to resting-
381 state pupil fluctuations is coupled to the BOLD signal in these areas. The main frequency band that drove our
382 pupil-AAS coupling was ~0.05-0.1 Hz. Interestingly, recent work in the mouse cortex has shown that the ultra-
383 slow (~0.1 Hz) BOLD fluctuations that are characteristic of resting-state fMRI data are entrained by ultra-slow
384 vasomotor oscillations that lead to rhythmic changes in the diameter of brain arterioles. These vasomotor
385 oscillations, in turn, are entrained by rhythmic local neuronal activity in the same ultra-low-frequency band (Drew
386 et al., 2020; Mateo et al., 2017). These findings beg the question whether this neurovascular coupling sequence
387 may be responsible for our findings. However, in the mouse brain this sequence, from neuronal activity and
388 vasomotion to blood oxygenation levels, was estimated to last approximately 2.6 s (Mateo et al., 2017). This
389 seems inconsistent with the 0- to 2-s interval between our estimated timing of the AAS neuronal activity
390 underlying pupil fluctuations and the timing of corresponding AAS BOLD signals. Future work in animal models
391 should therefore examine the physiological basis of these seemingly close temporal relationships between
392 activity of AAS nuclei and corresponding changes in pupil size by simultaneously measuring pupil size changes
393 and rhythmic BOLD fluctuations during awake rest.

394

395 Our study has several potential limitations. First, although our EPI sequence had a higher spatial
396 resolution (2 mm isotropic) than previous studies linking pupil size to BOLD (e.g., 3.5 mm isotropic in Murphy et
397 al., 2014), imaging small subcortical structures at this conventional spatial resolution may have led to partial-
398 volume averaging (Forstmann et al., 2017; Liu et al., 2017a), especially in the LC, the smallest of our ROIs. To
399 mitigate this concern, we did not apply spatial smoothing to the EPI data. Our confidence in the LC imaging data
400 reported here is also bolstered by the fact that the LC showed the same pattern of results as other, much larger
401 nuclei, including the VTA, SN and BF, that are less susceptible to partial-volume averaging effects. We also note
402 that a further increase in spatial resolution at 3T would be accompanied by a dramatic drop in signal-to-noise
403 ratio (Murphy et al., 2007), and therefore would not per se lead to a better signal from the AAS regions. Although
404 future studies combining pupillometry with ultra-high-field fMRI (e.g., 7T) could circumvent this problem,
405 measuring pupil size in ultra-high-field scanners is still challenging. A second potential limitation concerns the

406 proximity of some of the subcortical ROIs to air- and cerebrospinal fluid-filled cavities as well as major arteries,
407 making them particularly prone to movement and other sources of physiological noise (Brooks et al., 2013). To
408 mitigate this concern, we included an extensive physiological noise correction model, accounting for measured
409 cardiac and respiratory signal components as well as residual signal from the fourth ventricle. Furthermore, if
410 the BOLD signal in AAS nuclei was largely driven by noise, this could not explain the robust temporal relationship
411 between AAS BOLD and pupil size, and the selective absence of pupil-BOLD coupling in the pons, our control
412 region that is also susceptible to physiological noise artifacts. A third drawback is that our analyses were limited
413 by the temporal resolution of our fMRI data. Due to our 2-s TR we were unable to interrogate potentially
414 meaningful, faster pupil-BOLD correlations. Future studies using ultra-high-field fMRI and/or simultaneous
415 imaging techniques (Barth et al., 2016; Lewis et al., 2016) can speed up image acquisition and assess the presence
416 of pupil-BOLD correlations at a faster timescale.

417

418 In conclusion, we show that spontaneous changes in pupil size that occur during rest reflect activity in a
419 variety of nuclei that are part of the AAS. This suggests that pupil size can be used as a noninvasive and general
420 index of AAS activity, in contrast to previous work suggesting a selective role for the LC in arousal-related pupil
421 size changes. However, the nature of pupil-AAS coupling during rest appears to be vastly different from task-
422 related pupil-AAS coupling, which has previously been modeled using a canonical HRF. Together, our findings
423 provide new insights into the nature and temporal dynamics of AAS-linked pupil size fluctuations.

424

425 **Materials & Methods**

426 This study was preregistered on the Open Science Framework before data analysis: osf.io/xcj2y. Note
427 that preregistration occurred after data collection; due to circumstances surrounding the global pandemic,
428 already collected data was used to address our hypotheses. As we could not replicate previous findings, we
429 needed to deviate from the preregistration. When we deviated from the preregistration, this will be explicitly
430 mentioned below.

431

432 ***Participants***

433 Seventy-four right-handed participants were recruited from New York University (39 females, mean age:
434 22.5 years, age range: 18-33 years) and completed two resting-state sessions on two consecutive days. Exclusion
435 criteria for participation were as follows: current treatment or treatment in the last year of psychiatric,
436 neurological, or endocrine disease, current treatment with any medication, average use of >3 alcoholic beverages
437 daily, average use of recreational drugs, habitual smoking, uncorrected vision, and contraindications for MRI.
438 Two participants were excluded entirely and one session for one participant was excluded due to technical issues
439 with the scanner. The two resting-state sessions were part of a larger study of which the data will not be reported
440 here. The study was approved by the University Committee on Activities Involving Human Subjects at New York
441 University (Institutional Review Board #2016-2) and the study was conducted in accordance with these guidelines

442 and regulations. All participants provided written informed consent. Participants received a payment (\$35 per
443 hour) for their participation.

444

445 ***Procedure***

446 All participants completed two resting-state sessions of five minutes each, 24 hours apart (+/- 2 hours).
447 During the session they were instructed to think of nothing in particular, let their mind wander but not to have
448 any repetitive thoughts such as counting. They were instructed to keep their eyes open and maintain their gaze
449 on a centrally presented fixation dot (RGB: 60, 60, 255) on a grey screen (RGB: 125,125,125).

450

451 ***MRI data acquisition***

452 MRI data was acquired using a Siemens MAGNETOM Prisma 3T MR scanner. T2*-weighted BOLD images
453 were recorded using a customized multi-echo EPI sequence with ascending slice acquisition (58 axial slices; TR =
454 2 s; TE = 14.4, 39.1 ms; partial fourier = 6/8; GRAPPA acceleration factor = 2; multiband acceleration factor = 2;
455 flip angle = 65°; slice matrix size 104 x 104 mm; slice thickness = 2.0 mm; FOV: 208 x 208 mm; slice gap = 0;
456 bandwidth: 2090 Hz/px; echo spacing: 0.56 ms). Multi-echo EPI protocols can be used to avoid the tradeoff
457 between BOLD sensitivity in the cortex and subcortex (Turker et al., 2021). To account for regional variation in
458 susceptibility-induced signal dropout, voxel-wise weighted sums of both echoes were calculated based on local
459 contrast-to-noise ratio (Poser et al., 2006). A structural image (0.9 mm isotropic) was acquired using a T1-
460 weighted 3D MP-RAGE (TR = 2.3 s; TE = 2.32 ms; flip angle = 8°, FOV = 256 x 256 x 230 mm). A fast-spin echo (FSE)
461 neuromelanin-sensitive structural scan was acquired for delineation of the LC (11 axial slices , TR = 750 ms, TE =
462 10 ms, flip-angle = 120°, bandwidth = 220 Hz/Px, slice thickness = 2.5 mm, slice gap = 3.5 mm; in-plane resolution
463 = 0.429 x 0.429 mm). Note that a large slice gap is a common feature in the use of FSE scans for LC imaging (Liu
464 et al., 2017a). This procedure allows for a high in-plane resolution but with a thicker slice thickness, resulting in
465 elongated voxels that match the cylindrical shape of the LC. To minimize excessive movement during scanning,
466 we secured participants' heads in a pillow and medical tape was attached across their foreheads to provide
467 immediate tactile feedback in case of any movement, which has been shown to reduce motion (Krause et al.,
468 2019).

469

470 ***MRI data preprocessing***

471 Preprocessing of MRI data was carried out using Advanced Normalization Tools v2.1 (ANTs) and SPM12
472 (<https://www.fil.ion.ucl.ac.uk/spm>; Wellcome Department of Imaging Neuroscience, London, UK). Here we
473 deviated from the preregistration, as we reported we would carry out all preprocessing steps in SPM12. Since
474 ANTs SyN was found to be the best performing method for normalization (Ewert et al., 2019), some steps,
475 including standardization and registration, were carried out using ANTs instead,

476 A whole-brain group template ($T1_{template}$) was generated using all MP-RAGE scans (using
477 `antsMultivariateTemplateConstruction2.sh`; Figure S1a). This process involved two steps: 1) participants' whole-
478 brain T1 scans ($T1_{native\ space}$) were coregistered to a common group space ($T1_{group\ space}$); then 2) these coregistered
479 scans were averaged to form a whole-brain group template ($T1_{template}$). An initial fixed image was created by
480 averaging all input files. For registration (or 'normalization') of input images, a set of linear (rigid, then affine)
481 and nonlinear (SyN) algorithms were used. Each nonlinear registration was performed over four levels of
482 increasingly fine-grained resolutions (100x70x50x10 iterations). We applied a N4 bias field correction on moving
483 images before each registration (using `N4BiasFieldCorrection` function). Cross-correlation was the similarity
484 metric used for registration. Greedy SyN (SyN) was the transformation model used for registration. The gradient
485 step size for refining template updates was set at 0.20 mm. After the whole-brain template image ($T1_{template}$) was
486 generated, for optimal coregistration, all individual MP-RAGE scans ($T1_{native\ space}$) were submitted to a new
487 coregistration step (using `antsRegistration.sh`; Figure S1b). For this we performed linear (rigid, then affine),
488 followed by nonlinear (SyN), registration steps, resulting in optimized individual whole-brain scans in template
489 space ($T1_{group\ space}$).

490 Mutual information maximization-based rigid-body registration was used to register MP-RAGE scans
491 and functional images. Functional images were motion-corrected using rigid-body transformations. To move the
492 functional images into group space, the affine transforms and displacement field transformations from the final
493 coregistration ($T1_{native\ space}$ to $T1_{group\ space}$) for each participant were applied to their respective functional images
494 (using linear interpolation). To avoid contamination of AAS BOLD activity by signal from adjacent structures, all
495 analyses reported in this paper, except those aimed at replicating previous studies (see section '*Comparisons*
496 *with previous studies*'), were performed without spatial smoothing.

497 We applied a movement and physiological noise correction model with 33 regressors in SPM12. These
498 included six movement parameter regressors (3 translations, 3 rotations) derived from rigid-body motion
499 correction, high-pass filtering (1/128Hz cut-off) and AR(1) serial autocorrelation corrections. In addition these
500 included retrospective image-based correction (RETROICOR) of physiological noise artifacts (Glover et al., 2000)
501 regressors. Raw pulse was preprocessed using PulseCor (<https://github.com/lindvoo/PulseCor>) implemented in
502 Python for artifact correction and peak detection. Fifth-order Fourier models of the cardiac and respiratory
503 phase-related modulation of the BOLD signal were specified (Van Buuren et al., 2009), yielding 10 nuisance
504 regressors for cardiac noise and 10 for respiratory noise. Additional regressors were calculated for heart rate
505 frequency, heart rate variability, (raw) abdominal circumference, respiratory frequency, respiratory amplitude,
506 and respiration volume per unit time (Birn et al., 2006), yielding a total of 26 RETROICOR regressors
507 (<https://github.com/can-lab/RETROICORplus>). An additional regressor was added to remove signal fluctuations
508 from the fourth ventricle, which was manually delineated using individual MP-RAGE scans (M= 90, SD=34 voxels).
509 This movement and physiological noise correction model was added to all general linear models (GLMs)
510 described below. Please note that we deviated from the preregistration and did not apply 'scrubbing' in addition
511 to the 33 nuisance regressors.

512

513 ***Pupil data acquisition and preprocessing***

514 Pupil size was recorded using an MR-compatible eye-tracker (EyeLink 1000 Plus; SR Research, Osgoode,
515 ON, Canada) at a sampling rate of 250 Hz. The eye-tracker was placed at the end of the scanner bore, such that
516 the participant's right eye could be tracked via the head coil mirror. Before the start of each resting-state session,
517 we began with a calibration of the eye-tracker using the standard five-point EyeLink calibration procedure.

518 Moments when the eye-tracker received no pupil signal (i.e., during eye blinks) were marked
519 automatically during acquisition by the manufacturer's blink detection algorithm. Pupil data was preprocessed
520 using PupCor (<https://github.com/lindvoo/PupCor>) implemented in Python. Missing and invalid data due to
521 blinks were replaced using linear interpolation for the period from 100 ms before blink onset to 400 ms after
522 blink offset. Following the automated interpolation procedure, the data were manually checked and corrected if
523 any artifacts had not been successfully removed. Two sessions from two separate participants were excluded
524 due to technical problems with the eye-tracker. To ensure the pupil data was of good quality, a session was
525 excluded from all analyses if the raw pupil data contained >25% invalid samples (marked automatically during
526 data acquisition by EyeLink's blink detection algorithm; *n* sessions *excluded* = 15). For the remaining sessions (*n*
527 sessions *included* = 126; *n* participants = 70, average proportion invalid samples = 6.4%) we computed pupil size
528 as well as the first-order derivative of the pupil size time series. The latter describes the slope of changes in pupil
529 size, where positive values reflect pupil dilation and negative values reflect pupil constriction. Because pupil size
530 lags behind the underlying neural activity in AAS nuclei (including the LC and DR; Cazettes et al., 2021; Joshi et
531 al., 2016; Liu et al., 2017b; Reimer et al., 2016), and in line with previous neuroimaging studies (Pfeffer et al.,
532 2022; Schneider et al., 2016; Yellin et al., 2015), we shifted the pupil time series one second back in time. This
533 step was only omitted when we attempted to replicate Murphy et al. (2014). Both pupil time series (i.e., pupil
534 size and pupil derivative) were then resampled to the TR (2 s) resolution (0.5 Hz). To detect further artefactual
535 samples, within each 2-s time bin, any sample ± 3 SD outside the time bin mean was removed, after which the
536 average of the corresponding time bin was recalculated from the remaining non-artefactual samples (percentage
537 samples recalculated = 0.04%; as in Murphy et al., 2014). The results of these pre-processing steps were two
538 pupil time series (pupil size and pupil derivative) that were equal in length to the number of fMRI volumes (i.e.,
539 150) collected in each session.

540

541 ***Definition of regions-of-interest (ROIs)***

542 The LC was delineated on each participant's FSE scan using ITK-SNAP (version 3.8.0; Yushkevich et al.,
543 2006). Two raters (BL and a research assistant) manually identified LC voxels following established protocols
544 (Clewett et al., 2016; Mather et al., 2017). Pairwise dice similarity coefficients between both raters were high (*M*:
545 0.96, range: 0.70 – 1.00). As described in Clewett et al. (2016), left and right LC regions were identified in the
546 axial slice ~7 mm below the inferior colliculus. Within this slice, two regions were delineated in the form of a
547 cross ~1.29 mm wide and ~1.29 mm high (3 x 3 voxels, see Figure 2d), covering the 1 – 2 mm of LC neurons in
548 this slice. The center voxel for each cross was placed on the voxel with the highest signal intensity that fell within

549 an area anatomically consistent with the location of the LC. If the peak voxel was located immediately adjacent
550 to the fourth ventricle, the center of the ROI was placed one voxel further away from the ventricle. This ensured
551 that the peak voxel but no fourth ventricle voxels were included in the ROI. To ensure we captured LC intensity
552 signal, we calculated an objective measure for comparisons namely contrast-to-noise ratios between the average
553 signal intensity in the LC relative to a pontine reference region. Contrast-to-noise ratios were positive for all
554 participants, indicating that LC intensity was consistently higher than pontine intensity (M: 0.17, range: 0.08 –
555 0.29; Figure 2d). The obtained contrast-to-noise ratios were in line with previous reports (Clewett et al., 2016;
556 Mather et al., 2017). For three participants we could not delineate LC ROIs because movement led to poor-quality
557 FSE images. For these participants we used the group LC ROI (i.e., average of all individual LC ROIs in group space
558 thresholded at 2 SD above the mean). This group LC ROI was also used for visualization purposes. In line with
559 current standards (Yi et al., 2021), the LC masks were then transformed (using nearest neighbor interpolation)
560 into template space by applying the linear and nonlinear transformations from the final coregistration ($T1_{native}$
561 $space$ to $T1_{group\ space}$), and resliced resulting in the final individual LC masks in functional space (range of size in
562 functional space: 1 – 7 voxels, M=3.4, SD=1.3 voxels).

563 Published probabilistic atlases were used for the remaining subcortical ROIs as there are no established
564 protocols for individual segmentation of these regions: VTA (Trutti et al., 2021), SN (Alkemade et al., 2020), DR
565 (Beliveau et al., 2015), MR (Beliveau et al., 2015) and the sublenticular (Ch4) part of the BF (Eickhoff et al., 2005;
566 Zaborszky et al., 2008), which includes the cholinergic nucleus basalis of Meynert (see Figure 2a). All atlases were
567 originally in MNI space. To move the atlases into our study-specific template space, `antsRegistration.sh` (using
568 the same parameters as described above) was applied to generate the transformation matrices between MNI
569 space and template space, which were applied to each ROI mask. Each subcortical mask was then thresholded
570 and resliced to the functional space. In the preregistration, we reported that we would only be examining pupil-
571 BOLD coupling in the LC, VTA, and SN. We also opted to include the raphe nuclei and BF since recent evidence
572 shows that they are involved in driving pupil size during task behaviours (Cazettes et al., 2021; de Gee et al.,
573 2017).

574 Previous studies (Schneider et al., 2016; Yellin et al., 2015) have found a robust relationship between
575 pupil size and BOLD patterns in the occipital cortex (OCC) and anterior cingulate cortex (ACC). Therefore, we
576 included these two cortical regions as additional validation ROIs. Specifically, we obtained masks of the calcarine
577 sulcus in the OCC and ACC using the automated anatomical labeling atlas in SPM (Tzourio-Mazoyer et al., 2002).
578 Lastly, to explore the specificity of our pupil-AAS BOLD results, we delineated a cubic ROI in the medial part of
579 the basis pontis (pons), which served as a control region in which we did not expect to find pupil-BOLD coupling.
580 The same procedure as described above was carried out to move these masks from MNI space into our study-
581 specific template space.

582

583 ***fMRI data quality assessment***

584 *Comparisons with previous studies*

585 We wanted to ensure that we could replicate the resting-state correlations between pupil size and BOLD
586 patterns reported in previous studies. First, we followed the methods of Schneider et al. (2016). We convolved
587 the pupil size time series with the canonical HRF (6-s TTP [time-to-peak]). This single pupil regressor, along with
588 the movement and physiological noise correction model were entered into first-level GLMs. Note that we only
589 refer to the light condition in Schneider et al. (2016), since we did not assess other light conditions. Second, we
590 followed the methods of Murphy et al. (2014). Here, we used the preprocessed pupil size time series and
591 convolved that with the default canonical HRF, as well as its temporal and dispersion derivatives (Friston et al.,
592 2000). The resulting three pupil time series were entered into a first-level GLM together with the movement and
593 physiological noise correction model. For the Murphy et al. (2014) comparison analysis, the first-level single-
594 subject contrast maps were submitted to a second-level random effects analysis (one-way ANOVA, three levels
595 of pupil/basis functions). To interrogate pupil correlations within the LC, statistics were also carried at the
596 second-level using small volume correction with our group LC mask and the LC mask (Keren et al., 2009) used by
597 Murphy et al. (2014) as an ROI in SPM12. In line with the reports of Schneider et al. (2016) and Murphy et al.
598 (2014), the analyses described here included spatial smoothing with a 6-mm full width at half maximum (FWHM)
599 Gaussian kernel.

600

601 *Assessment of the quality of subcortical fMRI data*

602 Next, we assessed the signal quality within the subcortical nuclei to ensure we would be able to capture
603 pupil-AAS coupling. First, we inspected the temporal signal-to-noise ratio (tSNR) of our data in all cortical and
604 subcortical ROIs. To do this, the tSNR was calculated as the ratio of the mean and the standard deviation of the
605 signal across the unsmoothed BOLD time series from the two sessions. We then averaged the resulting tSNR
606 within each ROI. Second, we investigated if we could replicate previous work reporting co-fluctuations between
607 activity in various subcortical ROIs during rest (van den Brink et al., 2019). The extracted BOLD signal from each
608 ROI (LC, VTA, SN, DR, MR, BF, and pons as a control region) per session, per participant, was denoised (using the
609 movement and physiological noise correction model described above) and demeaned and then entered into a
610 partial correlation analysis. We computed a partial correlation for each pair of AAS nuclei, controlling for activity
611 in the pons. Correlation coefficients underwent a Fisher r -to- Z transform and were then submitted to one-sample
612 t -tests.

613

614 *Pupil-AAS coupling analyses*

615 To systematically examine pupil-AAS coupling, and to understand the temporal relationship between
616 the two signals, we conducted a set of three main analyses. The rationale for our approach was that previous
617 studies (see *Comparisons with previous studies*) assumed that pupil-brain coupling during rest would follow the
618 canonical HRF used in event-related fMRI designs. However, these assumptions may not be correct or may not
619 apply to subcortical nuclei. Therefore, in our first analysis we (i) convolved the pupil time series with participant-

620 specific and ROI-specific estimates of the HRF (described below in *Estimation of region- and participant-specific*
621 *HRF*), which showed a range of TTPs. In the second analysis we (ii) systematically changed the TTP of the canonical
622 HRF (from 1 to 6 s, in steps of 1 s) and convolved the pupil time series with each of these. And lastly, we (iii)
623 performed a pupil-AAS cross-correlation analysis in which we did not convolve the pupil time series at all. Note
624 that analyses (ii) and (iii) were not preregistered, as they were carried out to better understand the outcome of
625 analysis (i). Therefore, they should be deemed exploratory. We will now provide a detailed description of each
626 of these analyses.

627

628 *Estimation of region- and participant-specific HRF*

629 In the first main analysis, we aimed to account for HRF variability across different brain regions and
630 participants in our resting-state data. Here, we deviated from the preregistration, in which we stated that we
631 would obtain participant-specific HRFs from event-related fMRI data. However, the HRFs based on these event-
632 related fMRI data did not provide plausible HRFs in the AAS regions (i.e., did not rise up to one tall peak and
633 follow with an undershoot), possibly because these AAS regions may not have been involved in the task at hand.
634 Instead, we used a blind deconvolution technique developed by Wu et al. (2013) to estimate region- and
635 participant-specific HRFs based on the data from both resting-state sessions. This point process method has been
636 validated on simulated as well as empirical data (Rangaprakash et al., 2018; Wu et al., 2021). It assumes that a
637 common HRF is shared across various spontaneous point process events (i.e., random neural events) in a given
638 voxel or ROI. After physiological correction, the cleaned BOLD signal $y(t)$ at a given voxel or ROI is considered as
639 the convolution of the voxel/ROI-specific HRF $h(t)$ and spontaneous neural events $x(t)$

$$640 \quad y(t) = x(t) \otimes h(t) + c + \mathcal{E}(t)$$

641 where c is a constant term indicating the baseline magnitude of the BOLD response, $\mathcal{E}(t)$ is noise, and \otimes denotes
642 convolution. Spontaneous point process events $\hat{n}(t)$ were identified as BOLD fluctuations of relatively large
643 amplitude (one or more standard deviations away from the mean; see Figure 3a). Before identifying these events,
644 we removed movement and physiological noise with the same set of 33 regressors as described above (see *MRI*
645 *data preprocessing*). We then applied a high-pass filter (1/128Hz cut-off) and AR(1) serial autocorrelation
646 corrections. These events were modeled as a train of Dirac delta functions given by

$$647 \quad \hat{n}(t) = \sum_{\tau=0}^{\infty} \delta(t - \tau)$$

648 where $\delta(t - \tau)$ is the delta function. The ROI-specific HRF $h(t)$ was then fitted according to $\hat{n}(t)$ using a canonical
649 HRF and two derivatives (temporal derivative and dispersion derivative; Friston et al., 2000). Once $h(t)$ was
650 calculated, we obtained an approximation $\hat{n}(t)$ of the neural signal from the observed data using a Wiener filter.
651 ROI-specific HRFs (Figure 3b) were estimated for all AAS nuclei (i.e., LC, VTA, SN, DR, MR, BF) and two validation
652 regions (i.e., ACC, OCC) and one control region (i.e. pons). To maximize the number of spontaneous neural events,
653 HRFs were estimated based on the concatenated BOLD signals from the two sessions (see Figure 3c for number

654 of detected pseudo-events per ROI). These HRFs were then convolved with the two pupil time series (i.e., pupil
655 size [Figure 3e] and pupil derivative [Figure 3f]), forming the final pupil regressors that were entered into the
656 GLMs for this analysis. GLMs were made up of a single pupil regressor-of-interest in addition to our physiological
657 noise correction model described above. Analysis for pupil size included nine GLMs per participant, dedicated to
658 six AAS nuclei (LC, VTA, SN, DR, MR, BF) and the three validation and control regions (ACC, OCC, pons). Similarly,
659 nine models formed the analysis for the pupil derivative.

660

661 *Systematic adjustment of HRF time-to-peak*

662 To explore other possible temporal relationships between pupil size and AAS BOLD patterns, we carried
663 out a second analysis of pupil-AAS coupling where the TTP of the HRF was systematically shifted in time (*time-*
664 *to-peak [TTP] analysis*; Pais-Roldán et al., 2020). This was done using the canonical HRF (Friston et al., 2000),
665 which by default has a TTP (delay of response relative to onset) of 6 s. To explore pupil-AAS coupling at shorter
666 lags, we compared six HRFs with TTPs varying between 1, 2, 3, 4, 5, and 6 s. These HRFs were created using
667 `spm_hrf()` in SPM, where parameter $p(1)$ which refers to ‘delay of response (relative to onset)’ was adjusted from
668 6 (default) to 1, 2, 3, 4, and 5 respectively. Note that the 6-s TTP corresponds to the TTP used in the analysis
669 corresponding to Schneider et al. (2016). These six HRFs were then convolved with the two pupil time series
670 (pupil size, pupil derivative) for each participant, resulting in 12 pupil regressors. Each pupil size regressor was
671 then added to the physiological noise correction model, making up six GLMs per participant, each focusing on
672 one TTP (i.e., 1 s, 2 s, 3 s, 4 s, 5 s, 6 s). Similarly, six GLMs were created for the pupil derivative.

673

674 *Analyses using unconvolved pupil time series*

675 To further characterize the nature of pupil-AAS coupling we carried out two analyses using the
676 *unconvolved* pupil time series. Firstly, we performed a cross-correlation analysis (Pais-Roldán et al., 2020) in
677 which the preprocessed (downsampled, demeaned, unconvolved) pupil timeseries (size and derivative) were
678 shifted forwards and backwards relative to the BOLD signal (denoised using the movement and physiological
679 noise correction model and demeaned). Note that the BOLD signal from each ROI was first averaged and then
680 entered into the cross-correlation analysis. This analysis is similar to the TTP analysis but used unconvolved pupil
681 time series and allowed us to investigate both positive and negative lags between the pupil and BOLD signals,
682 which was not possible with the TTP method. Secondly, in order to determine which frequencies were driving
683 the observed pupil-BOLD cross-correlations, we estimated for each ROI the cross spectral power density (Yellin
684 et al., 2015), the Fourier transform of the cross-correlations. We did this using `cspd()` in Matlab, setting the
685 window length to 10 samples with an overlap of 3 samples.

686

687 **Statistical analyses**

688 All first-level GLMs described above were constructed in SPM12 with session (session 1, session 2) as a
689 within-subject factor (n=56). For participants in which only one session could be included (i.e., due to pupil quality
690 exclusion criteria or technical issues in a scanning session), a GLM was constructed using only one session (n =
691 14).

692 Second-level analyses were carried out by extracting *t*-values from single-subject contrast maps
693 generated from the first-level analyses. These weights were then submitted to a second-level random effects
694 analysis (one-sample *t*-test) in R using ‘stats’ package. To correct for multiple comparisons, alpha levels (set at
695 0.05) were adjusted by controlling the false discovery rate (FDR).

696 For the comparison analyses with Schneider et al. (2016) and Murphy et al. (2014), single-subject
697 contrast maps obtained from first-level analyses were entered into second-level random effects analyses (one-
698 sample *t*-test for Schneider et al. [2016] and a one-way repeated-measures analysis of variance [ANOVA] with
699 three levels for Murphy et al. [2014]) in SPM12. Here, we used a cluster-forming voxel-level threshold of $p < .001$
700 (uncorrected). Alpha was set at 0.05 whole-brain family-wise error (FWE) corrected at the cluster level using
701 Gaussian random field theory-based methods as implemented in SPM12 (Friston et al., 1996).

702

703 **Data and code availability statement**

704 Analyses code can be found here: https://github.com/bethlloyd/rs-fMRI_brainstem. Brain maps and processed
705 pupil time series data will be uploaded to <https://osf.io/9fkzp/> upon publication.

706

707 **Declarations of interest**

708 Authors declare that they have no conflict of interest.

709

710 **Credit authorship and contribution statement**

711 **Beth Lloyd:** Conceptualization, Methodology, Software, Validation, Formal analysis, Investigation, Data
712 Curation, Writing – Original Draft, Visualization. **Lycia D. de Voogd:** Conceptualization, Methodology, Software,
713 Investigation, Data Curation, Writing – Review & Editing. **Verónica Mäki-Marttunen:** Conceptualization,
714 Methodology, Supervision, Writing – Review & Editing. **Sander Nieuwenhuis:** Conceptualization, Methodology,
715 Resources, Writing – Review & Editing, Supervision, Funding acquisition.

716

717 **Acknowledgements**

718 Data collection was funded by the Templeton World Charity Foundation, Inc. network “Survival Circuits
719 Influences on Human Nature” to LdV, Elizabeth Phelps and Joseph LeDoux. This publication is part of a Vici project

720 (with project number VI.C.181.032) that is financed by the Dutch Research Council (NWO) awarded to Sander
721 Nieuwenhuis. We would also like to thank Birte Forstmann and Steven Miletic for their helpful contributions.

722

723 **References**

724 Alkemade, A., Mulder, M. J., Groot, J. M., Isaacs, B. R., Van, N., Lute, N., Js, S., Bazin, P., & Forstmann, B. U.
725 (2020). NeuroImage The Amsterdam Ultra-high field adult lifespan database (AHEAD): A freely
726 available multimodal 7 Tesla submillimeter magnetic resonance imaging database. *NeuroImage*,
727 221(July), 117200. <https://doi.org/10.1016/j.neuroimage.2020.117200>

728 Beliveau, V., Svarer, C., Frokjaer, V. G., Knudsen, G. M., Greve, D. N., & Fisher, P. M. (2015). Functional
729 connectivity of the dorsal and median raphe nuclei at rest. *NeuroImage*.
730 <https://doi.org/10.1016/j.neuroimage.2015.04.065>

731 Birn, R. M., Diamond, J. B., Smith, M. A., & Bandettini, P. A. (2006). Separating respiratory-variation-related
732 fluctuations from neuronal-activity-related fluctuations in fMRI. *NeuroImage*, 31(4), 1536–1548.
733 <https://doi.org/10.1016/j.neuroimage.2006.02.048>

734 Breeden, A. L., Siegle, G. J., Norr, M. E., Gordon, E. M., & Vaidya, C. J. (2016). *Coupling between spontaneous*
735 *pupillary fluctuations and brain activity relates to inattentiveness*. 1–7. <https://doi.org/10.1111/ejn.13424>

736 Breton-provencher, V., & Sur, M. (2019). Active control of arousal by a locus coeruleus GABAergic circuit.
737 *Nature Neuroscience*, 22(February). <https://doi.org/10.1038/s41593-018-0305-z>

738 Brooks, J. C. W., Faull, O. K., Pattinson, K. T. S., & Jenkinson, M. (2013). Physiological noise in brainstem fMRI.
739 *Frontiers in Human Neuroscience*, c(OCT), 1–13. <https://doi.org/10.3389/fnhum.2013.00623>

740 Bunzeck, N., & Düzel, E. (2006). Absolute Coding of Stimulus Novelty in the Human Substantia Nigra/VTA.
741 *Neuron*. <https://doi.org/10.1016/j.neuron.2006.06.021>

742 Cazettes, F., Reato, D., Morais, J. P., Renart, A., & Mainen, Z. F. (2021). Phasic Activation of Dorsal Raphe
743 Serotonergic Neurons Increases Pupil Size. *Current Biology*. <https://doi.org/10.1016/j.cub.2020.09.090>

744 Cazettes, F., Reato, D., Morais, P., Renart, A., Mainen, Z. F., Morais, P., Renart, A., & Mainen, Z. F. (2021).
745 *Report Phasic Activation of Dorsal Raphe Serotonergic Neurons Increases Pupil Size II II Phasic Activation*
746 *of Dorsal Raphe Serotonergic Neurons Increases Pupil Size*. 192–197.
747 <https://doi.org/10.1016/j.cub.2020.09.090>

748 Clewett, D. V., Lee, T. H., Greening, S., Ponzio, A., Margalit, E., & Mather, M. (2016). Neuromelanin marks the
749 spot: identifying a locus coeruleus biomarker of cognitive reserve in healthy aging. *Neurobiology of Aging*,
750 37, 117–126. <https://doi.org/10.1016/j.neurobiolaging.2015.09.019>

751 Colizoli, O., Gee, J. W. De, van der Zwaag, W., & Donner, T. H. (2022). Functional magnetic resonance imaging

- 752 responses during perceptual decision-making at 3 and 7 T in human cortex , striatum , and brainstem.
753 *Human Brain Mapping*, 43(4), 1265–1279. <https://doi.org/10.1002/hbm.25719>
- 754 de Gee, J. W., Colizoli, O., Kloosterman, N. A., Knäpen, T., Nieuwenhuis, S., & Donner, T. H. (2017). Dynamic
755 modulation of decision biases by brainstem arousal systems. *ELife*. <https://doi.org/10.7554/eLife.23232>
- 756 DiNuzzo, M., Mascali, D., Moraschi, M., Bussu, G., Maugeri, L., Mangini, F., Fratini, M., & Giove, F. (2019). Brain
757 Networks Underlying Eye’s Pupil Dynamics. *Frontiers in Neuroscience*.
758 <https://doi.org/10.3389/fnins.2019.00965>
- 759 Drew, P. J., Mateo, C., Turner, K. L., Yu, X., & Kleinfeld, D. (2020). Perspective Ultra-slow Oscillations in fMRI and
760 Resting-State Connectivity : Neuronal and Vascular Contributions and Technical Confounds. *Neuron*,
761 107(5), 782–804. <https://doi.org/10.1016/j.neuron.2020.07.020>
- 762 Eickhoff, S. B., Stephan, K. E., Mohlberg, H., Grefkes, C., Fink, G. R., Amunts, K., & Zilles, K. (2005). A new SPM
763 toolbox for combining probabilistic cytoarchitectonic maps and functional imaging data. *NeuroImage*.
764 <https://doi.org/10.1016/j.neuroimage.2004.12.034>
- 765 Ewert, S., Horn, A., Finkel, F., Li, N., Kühn, A. A., & Herrington, T. M. (2019). Optimization and comparative
766 evaluation of nonlinear deformation algorithms for atlas-based segmentation of DBS target nuclei.
767 *NeuroImage*. <https://doi.org/10.1016/j.neuroimage.2018.09.061>
- 768 Forstmann, B. U., De Hollander, G., Van Maanen, L., Alkemade, A., & Keuken, M. C. (2017). Towards a
769 mechanistic understanding of the human subcortex. *Nature Reviews Neuroscience*, 18(1), 57–65.
770 <https://doi.org/10.1038/nrn.2016.163>
- 771 Friston, K. J., Holmes, A., Poline, J. B., Price, C. J., & Frith, C. D. (1996). Detecting activations in pet and fMRI:
772 Levels of inference and power. *NeuroImage*. <https://doi.org/10.1006/nimg.1996.0074>
- 773 Friston, K. J., Mechelli, A., Turner, R., & Price, C. J. (2000). Nonlinear responses in fMRI: The balloon model,
774 Volterra kernels, and other hemodynamics. *NeuroImage*. <https://doi.org/10.1006/nimg.2000.0630>
- 775 Glover, G. H., Li, T. Q., & Ress, D. (2000). Image-based method for retrospective correction of physiological
776 motion effects in fMRI: RETROICOR. *Magnetic Resonance in Medicine*. [https://doi.org/10.1002/1522-2594\(200007\)44:1<162::AID-MRM23>3.0.CO;2-E](https://doi.org/10.1002/1522-2594(200007)44:1<162::AID-MRM23>3.0.CO;2-E)
- 778 Handwerker, D. A., Ollinger, J. M., & D’Esposito, M. (2004). Variation of BOLD hemodynamic responses across
779 subjects and brain regions and their effects on statistical analyses. *NeuroImage*.
780 <https://doi.org/10.1016/j.neuroimage.2003.11.029>
- 781 Harvey, A. K., Pattinson, K. T. S., Brooks, J. C. W., Mayhew, S. D., Jenkinson, M., & Wise, R. G. (2008). Brainstem
782 functional magnetic resonance imaging: Disentangling signal from physiological noise. *Journal of*
783 *Magnetic Resonance Imaging*. <https://doi.org/10.1002/jmri.21623>
- 784 Joshi, S., & Gold, J. I. (2020). Pupil Size as a Window on Neural Substrates of Cognition. In *Trends in Cognitive*

- 785 *Sciences*. <https://doi.org/10.1016/j.tics.2020.03.005>
- 786 Joshi, S., Li, Y., Kalwani, R. M., & Gold, J. I. (2016). Relationships between Pupil Diameter and Neuronal Activity
787 in the Locus Coeruleus, Colliculi, and Cingulate Cortex. *Neuron*.
788 <https://doi.org/10.1016/j.neuron.2015.11.028>
- 789 Keren, N. I., Lozar, C. T., Harris, K. C., Morgan, P. S., & Eckert, M. A. (2009). In vivo mapping of the human locus
790 coeruleus. *NeuroImage*. <https://doi.org/10.1016/j.neuroimage.2009.06.012>
- 791 Keren, N. I., Taheri, S., Vazey, E. M., Morgan, P. S., Granholm, A. C. E., Aston-Jones, G. S., & Eckert, M. A. (2015).
792 Histologic validation of locus coeruleus MRI contrast in post-mortem tissue. *NeuroImage*, *113*, 235–245.
793 <https://doi.org/10.1016/j.neuroimage.2015.03.020>
- 794 Krause, F., Benjamins, C., Eck, J., Lührs, M., van Hoof, R., & Goebel, R. (2019). Active head motion reduction in
795 magnetic resonance imaging using tactile feedback. *Human Brain Mapping*, *40*(14), 4026–4037.
796 <https://doi.org/10.1002/hbm.24683>
- 797 Lau, C., Zhou, I. Y., Cheung, M. M., Chan, K. C., & Wu, E. X. (2011). BOLD temporal dynamics of rat superior
798 colliculus and lateral geniculate nucleus following short duration visual stimulation. *PLoS ONE*.
799 <https://doi.org/10.1371/journal.pone.0018914>
- 800 Lewis, L. D., Setsompop, K., Rosen, B. R., & Polimeni, J. R. (2018). Stimulus-dependent hemodynamic response
801 timing across the human subcortical-cortical visual pathway identified through high spatiotemporal
802 resolution 7T fMRI. *NeuroImage*. <https://doi.org/10.1016/j.neuroimage.2018.06.056>
- 803 Liu, K. Y., Marijatta, F., Hämmerer, D., Acosta-Cabronero, J., Düzel, E., & Howard, R. J. (2017a). Magnetic
804 resonance imaging of the human locus coeruleus: A systematic review. *Neuroscience and Biobehavioral*
805 *Reviews*, *83*(September), 325–355. <https://doi.org/10.1016/j.neubiorev.2017.10.023>
- 806 Liu, K. Y., Marijatta, F., Hämmerer, D., Acosta-Cabronero, J., Düzel, E., & Howard, R. J. (2017b). Magnetic
807 resonance imaging of the human locus coeruleus: A systematic review. *Neuroscience and Biobehavioral*
808 *Reviews*, *83*(June), 325–355. <https://doi.org/10.1016/j.neubiorev.2017.10.023>
- 809 Mäki-Marttunen, V., & Espeseth, T. (2021). Uncovering the locus coeruleus: Comparison of localization
810 methods for functional analysis. *NeuroImage*. <https://doi.org/10.1016/j.neuroimage.2020.117409>
- 811 Mateo, C., Knutsen, P. M., Tsai, P. S., & Shih, A. Y. (2017). Entrainment of Arteriole Vasomotor Fluctuations by
812 Neural Activity Is a Basis of Blood-Oxygenation- Article Entrainment of Arteriole Vasomotor Fluctuations
813 by Neural Activity Is a Basis of Blood-Oxygenation-. *Neuron*, *96*(4), 936-948.e3.
814 <https://doi.org/10.1016/j.neuron.2017.10.012>
- 815 Mather, M., Joo Yoo, H., Clewett, D. V., Lee, T. H., Greening, S. G., Ponzio, A., Min, J., & Thayer, J. F. (2017).
816 Higher locus coeruleus MRI contrast is associated with lower parasympathetic influence over heart rate
817 variability. *NeuroImage*, *150*(November 2016), 329–335.

- 818 <https://doi.org/10.1016/j.neuroimage.2017.02.025>
- 819 Matt, E., Fischmeister, F. P. S., Amini, A., Robinson, S. D., Weber, A., Foki, T., Gizewski, E. R., & Beisteiner, R.
820 (2019). Improving sensitivity, specificity, and reproducibility of individual brainstem activation. *Brain*
821 *Structure and Function*, 224(8), 2823–2838. <https://doi.org/10.1007/s00429-019-01936-3>
- 822 Megemont, M., & Mcburney, J. (2022). Pupil diameter is not an accurate real- - time readout of locus
823 coeruleus activity. *ELife*, 11, e70510.
- 824 Miletić, S., Bazin, P. L., Weiskopf, N., van der Zwaag, W., Forstmann, B. U., & Trampel, R. (2020). fMRI protocol
825 optimization for simultaneously studying small subcortical and cortical areas at 7 T. *NeuroImage*,
826 219(December 2019). <https://doi.org/10.1016/j.neuroimage.2020.116992>
- 827 Murphy, P. R., O’Connell, R. G., O’Sullivan, M., Robertson, I. H., & Balsters, J. H. (2014). Pupil diameter covaries
828 with BOLD activity in human locus coeruleus. *Human Brain Mapping*. <https://doi.org/10.1002/hbm.22466>
- 829 Pais-Roldán, P., Takahashi, K., Sobczak, F., Chen, Y., Zhao, X., Zeng, H., Jiang, Y., & Yu, X. (2020). Indexing brain
830 state-dependent pupil dynamics with simultaneous fMRI and optical fiber calcium recording. *Proceedings*
831 *of the National Academy of Sciences of the United States of America*.
832 <https://doi.org/10.1073/pnas.1909937117>
- 833 Pfeffer, T., Keitel, C., Kluger, D. S., Keitel, A., Russmann, A., Thut, G., Donner, T. H., & Gross, J. (2022). Coupling
834 of pupil-and neuronal population dynamics reveals diverse influences of arousal on cortical processing.
835 *ELife*, 11, 1–28. <https://doi.org/10.7554/ELIFE.71890>
- 836 Poser, B. A., Versluis, M. J., Hoogduin, J. M., & Norris, D. G. (2006). BOLD contrast sensitivity enhancement and
837 artifact reduction with multiecho EPI: Parallel-acquired inhomogeneity-desensitized fMRI. *Magnetic*
838 *Resonance in Medicine*, 55(6), 1227–1235. <https://doi.org/10.1002/mrm.20900>
- 839 Priovoulos, N., Jacobs, H. I. L., Ivanov, D., Uludağ, K., Verhey, F. R. J., & Poser, B. A. (2018). High-resolution in
840 vivo imaging of human locus coeruleus by magnetization transfer MRI at 3T and 7T. *NeuroImage*.
841 <https://doi.org/10.1016/j.neuroimage.2017.07.045>
- 842 Puckett, A. M., Bollmann, S., Poser, B. A., Palmer, J., Barth, M., & Cunnington, R. (2018). NeuroImage Using
843 multi-echo simultaneous multi-slice (SMS) EPI to improve functional MRI of the subcortical nuclei of the
844 basal ganglia at ultra-high field (7T). *NeuroImage*, 172(December 2017), 886–895.
845 <https://doi.org/10.1016/j.neuroimage.2017.12.005>
- 846 Rangaprakash, D., Wu, G. R., Marinazzo, D., Hu, X., & Deshpande, G. (2018). Hemodynamic response function
847 (HRF) variability confounds resting-state fMRI functional connectivity. *Magnetic Resonance in Medicine*.
848 <https://doi.org/10.1002/mrm.27146>
- 849 Reimer, J., McGinley, M. J., Liu, Y., Rodenkirch, C., Wang, Q., McCormick, D. A., & Tolia, A. S. (2016). Pupil
850 fluctuations track rapid changes in adrenergic and cholinergic activity in cortex. *Nature Communications*.

- 851 <https://doi.org/10.1038/ncomms13289>
- 852 Schneider, M., Hathway, P., Leuchs, L., Sämann, P. G., Czisch, M., & Spormaker, V. I. (2016). Spontaneous pupil
853 dilations during the resting state are associated with activation of the salience network. *NeuroImage*.
854 <https://doi.org/10.1016/j.neuroimage.2016.06.011>
- 855 Shine, J. M., Müller, E. J., Munn, B., Cabral, J., Moran, R. J., & Breakspear, M. (2021). Computational models link
856 cellular mechanisms of neuromodulation to large-scale neural dynamics. In *Nature Neuroscience*.
857 <https://doi.org/10.1038/s41593-021-00824-6>
- 858 Singh, K., Cauzzo, S., García-gomar, M. G., Stauder, M., Vanello, N., Passino, C., & Bianciardi, M. (2022).
859 *NeuroImage Functional connectome of arousal and motor brainstem nuclei in living humans by 7 Tesla*
860 *resting-state fMRI*. 249(November 2021). <https://doi.org/10.1016/j.neuroimage.2021.118865>
- 861 Thiele, A., & Bellgrove, M. A. (2018). Neuromodulation of Attention. In *Neuron*.
862 <https://doi.org/10.1016/j.neuron.2018.01.008>
- 863 Trutti, A. C., Fontanesi, L., Mulder, M. J., Bazin, P. L., Hommel, B., & Forstmann, B. U. (2021). A probabilistic
864 atlas of the human ventral tegmental area (VTA) based on 7 Tesla MRI data. *Brain Structure and Function*.
865 <https://doi.org/10.1007/s00429-021-02231-w>
- 866 Turker, H. B., Riley, E., Luh, W. M., Colcombe, S. J., & Swallow, K. M. (2021). Estimates of locus coeruleus
867 function with functional magnetic resonance imaging are influenced by localization approaches and the
868 use of multi-echo data. *NeuroImage*. <https://doi.org/10.1016/j.neuroimage.2021.118047>
- 869 Tzourio-Mazoyer, N., Landeau, B., Papathanassiou, D., Crivello, F., Etard, O., Delcroix, N., Mazoyer, B., & Joliot,
870 M. (2002). Automated anatomical labeling of activations in SPM using a macroscopic anatomical
871 parcellation of the MNI MRI single-subject brain. *NeuroImage*, 15(1), 273–289.
872 <https://doi.org/10.1006/nimg.2001.0978>
- 873 Van Buuren, M., Gladwin, T. E., Zandbelt, B. B., Van Den Heuvel, M., Ramsey, N. F., Kahn, R. S., & Vink, M.
874 (2009). Cardiorespiratory effects on default-mode network activity as measured with fMRI. *Human Brain*
875 *Mapping*, 30(9), 3031–3042. <https://doi.org/10.1002/hbm.20729>
- 876 Van den Brink, R., Colizoli, O., de Gee, J. W., Donner, T. H., (2019/11). Neuromodulatory brainstem activity
877 predicts intrinsic co-fluctuations in cortical activity. *Society for Neuroscience*.
- 878 Varazzani, C., San-Galli, A., Gilardeau, S., & Bouret, S. (2015). Noradrenaline and dopamine neurons in the
879 reward/effort trade-off: A direct electrophysiological comparison in behaving monkeys. *Journal of*
880 *Neuroscience*. <https://doi.org/10.1523/JNEUROSCI.0454-15.2015>
- 881 Wall, M. B., Walker, R., & Smith, A. T. (2009). Functional imaging of the human superior colliculus: An optimised
882 approach. *NeuroImage*. <https://doi.org/10.1016/j.neuroimage.2009.05.094>
- 883 Wu, G. R., Colenbier, N., Van Den Bossche, S., Clauw, K., Johri, A., Tandon, M., & Marinazzo, D. (2021). rsHRF: A

- 884 toolbox for resting-state HRF estimation and deconvolution. *NeuroImage*, 244(June).
885 <https://doi.org/10.1016/j.neuroimage.2021.118591>
- 886 Wu, G. R., Liao, W., Stramaglia, S., Ding, J. R., Chen, H., & Marinazzo, D. (2013). A blind deconvolution approach
887 to recover effective connectivity brain networks from resting state fMRI data. *Medical Image Analysis*.
888 <https://doi.org/10.1016/j.media.2013.01.003>
- 889 Yang, H., Bari, B. A., Cohen, J. Y., & O'Connor, D. H. (2021). Locus coeruleus spiking differently correlates with s1
890 cortex activity and pupil diameter in a tactile detection task. *ELife*. <https://doi.org/10.7554/eLife.64327>
- 891 Yellin, D., Berkovich-ohana, A., & Malach, R. (2015). NeuroImage Coupling between pupil fluctuations and
892 resting-state fMRI uncovers a slow build-up of antagonistic responses in the human cortex. *NeuroImage*,
893 106, 414–427. <https://doi.org/10.1016/j.neuroimage.2014.11.034>
- 894 Yen, C. C. C., Fukuda, M., & Kim, S. G. (2011). BOLD responses to different temporal frequency stimuli in the
895 lateral geniculate nucleus and visual cortex: Insights into the neural basis of fMRI. *NeuroImage*.
896 <https://doi.org/10.1016/j.neuroimage.2011.06.022>
- 897 Yi, Y.-J., Lüsebrink, F., Maaß, A., Ziegler, G., Yakupov, R., Kreißl, M. C., Betts, M., Speck, O., Düzel, E., &
898 Hämmerer, D. (2021). It is the Locus Coeruleus! Or... is it? : A proposition for analyses and reporting
899 standards for structural and functional magnetic resonance imaging of the noradrenergic Locus
900 Coeruleus. *BioRxiv*, 2021.10.01.462807. <https://doi.org/10.1101/2021.10.01.462807>
- 901 Yushkevich, P. A., Piven, J., Hazlett, H. C., Smith, R. G., Ho, S., Gee, J. C., & Gerig, G. (2006). User-guided 3D
902 active contour segmentation of anatomical structures: Significantly improved efficiency and reliability.
903 *NeuroImage*, 31(3), 1116–1128. <https://doi.org/10.1016/j.neuroimage.2006.01.015>
- 904 Zaborszky, L., Hoemke, L., Mohlberg, H., Schleicher, A., Amunts, K., & Zilles, K. (2008). Stereotaxic probabilistic
905 maps of the magnocellular cell groups in human basal forebrain. *NeuroImage*, 42(3), 1127–1141.
906 <https://doi.org/10.1016/j.neuroimage.2008.05.055>
- 907